Computational Study of NASA's Quadrotor Urban Air Taxi Concept

Patricia Ventura Diaz* and Seokkwan Yoon†
NASA Ames Research Center, Moffett Field, California

High-fidelity computational fluid dynamics simulations have been carried out in order to analyze NASA's quadrotor urban air taxi concept for urban air mobility, also know as on-demand mobility applications. High-order accurate schemes, dual-time stepping, and the delayed detached-eddy simulation model have been employed. The flow solver has been loosely coupled with a rotorcraft comprehensive analysis code. The vehicle simulated is a six-passenger quadrotor for air taxi operations. A study of power reduction as a function of the rear-rotor to front-rotors vertical separation has been performed, for a quad-rotor without the airframe, in cruise flight conditions. Then, the quadrotor without the airframe has been simulated in hover. The airloads and wake geometries are analyzed. To finish the study the complete quadrotor vehicle is presented. NASA's quadrotor air taxi concept is one of the many concepts being developed by NASA in support of aircraft development for vertical take-off and landing air taxi operations.

Nomenclature

T	Rotor thrust
P	Rotor power
Q	Rotor torque
C_T	Thrust coefficient, $\frac{T}{\rho A(\Omega R)^2}$
C_P	Power coefficient, $\frac{P}{\rho A(\Omega R)^3}$
C_Q	Torque coefficient, $\frac{Q}{\rho A(\Omega R)^2 R}$
C'	Sectional chord force
N'	Sectional blade normal force
M'	Sectional blade pitching moment
M^2c_c	Sectional chord force coefficient, $\frac{C'}{\frac{1}{2}\rho a^2 c}$
M^2c_n	Sectional normal force coefficient, $\frac{N'}{\frac{1}{2}\rho a^2 c}$
M^2c_m	Sectional pitching moment coefficient, $\frac{M'}{\frac{1}{2}\rho a^2 c^2}$
M	Mach number, $\frac{V}{a}$
M_{tip}	Mach number at the blade tip, $\frac{\Omega R}{a}$
Re	Reynolds number, $\frac{V L_{ref}}{\nu}$
Re_{tip}	Reynolds number at the blade tip, $\frac{\Omega R c_{tip}}{\nu}$
a	Fluid speed of sound
d	Turbulent length scale
y^+	Non-dimensional viscous wall spacing
A	Rotor disk area
R	Rotor radius
r	Radial position
c	Local rotor blade chord length
V_∞	Freestream velocity
α	Angle of Attack (AoA)
β_0	Coning angle
β_{1c}	Longitudinal flapping angle
β_{1s}	Lateral flapping angle
θ_0	Collective angle
θ_{1c}	Lateral cyclic pitch
θ_{1s}	Longitudinal cyclic pitch
ψ	Azimuth position
δ	Boundary layer thickness
μ	Advance ratio, $\frac{V_\infty cos(\alpha)}{\Omega R}$
σ	Rotor solidity
ν	Fluid kinematic viscosity
ρ	Fluid density
Δ	Grid spacing
Ω	Rotor rotational speed

Subscript

root	Blade root
tip	Blade tip
∞	Freestream

*Science & Technology Corporation
†NASA Advanced Supercomputing Division

I. Introduction

Advanced air mobility vehicles, also known as urban air taxis, or eVTOL (electric Vertical Take-Off and Landing) aircraft, are conceived to be the future means of transportation in the urban areas. With air taxis, the travel time will be drastically reduced in highly congested cities. In addition, by using hybrid or electric propulsion, these vehicles will provide a greener means of transportation. This goal in air transportation is known as Urban Air Mobility (UAM).

The accurate prediction of rotorcraft performance and acoustics is very challenging from a computational point of view: the flows are unsteady, nonlinear and complex. In the case of multi-rotor vehicles, the aerodynamic interactions between the rotors (and other components when simulating the complete vehicle) make the problem even more difficult. While low-fidelity tools offer the advantage of a short turn-around and low computational cost, only with high-fidelity methods the complex flow details and the aerodynamic interactions can be captured. In addition, high-fidelity simulations can provide the information needed to calibrate the lower fidelity tools that can be used for design purposes.

Previous high-fidelity Computational Fluid Dynamics (CFD) work performed by Ventura Diaz *et al.*[1–4] and Yoon *et al.*[5] includes simulations of NASA's side-by-side air taxi concept,[1] ducted and coaxial rotors,[2] and computational analysis of small multi-rotor vehicles.[3–5]

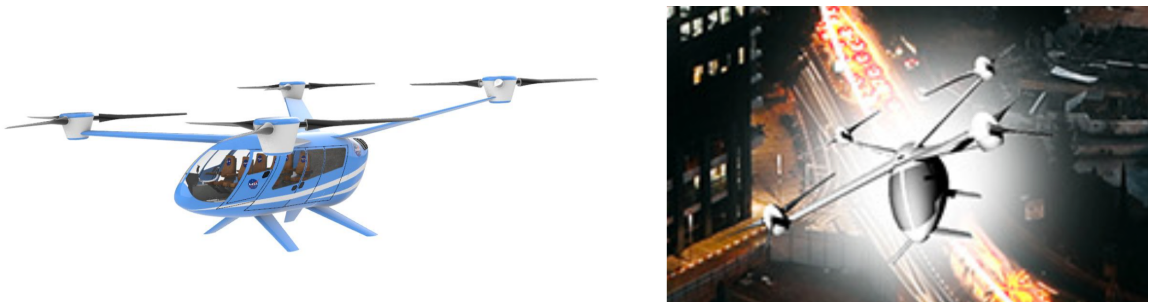

Figure 1: NASA's quadcopter UAM concept.

Johnson and Silva[6] conducted a comprehensive analysis study using Multidisciplinary Design, Analysis, and Optimization (MDAO) techniques, for several multi-rotor vehicles, including different concept vehicles for the UAM mission: a quadrotor, a side-by-side helicopter, or a lift+cruise VTOL vehicle, to name a few of them.

The objectives of the present work are to simulate and analyze NASA's quadrotor UAM concept using high-fidelity CFD. First, the results of the quadrotor "only-rotors" configuration (without the fuselage) will be presented. The quadcopter simulations using high-fidelity CFD are loosely coupled with a comprehensive rotorcraft code for accurate prediction of blade motions and airloads. A study of the effect of the vertical separation between the front and the rear rotors in cruise is performed. The "rotors-only" configuration will then be simulated in hover. Then, the complete vehicle results will be examined. The rotor wake geometry, airloads, and performance are analyzed for each case.

Although there are no validation data for these simulations, the computations might assist in future validation testing.

II. Numerical Approach

The flow solver used in this study is NASA's Overflow[7] CFD solver. Overflow is a finite-difference, structured overset grid, high-order accurate Navier-Stokes flow solver. NASA's Chimera Grid Tools (CGT)[8] overset grid generation software is used for generating the overset grids of rotors and complete vehicles. Body-fitted curvilinear Near-Body (NB) grids are generated using CGT. The computational domain is completed with the generation of Cartesian Off-Body (OB) grids that are automatically generated prior to grid assembly using the domain connectivity framework in Overflow-D mode. The current time-accurate approach consists of an inertial coordinate system where NB curvilinear O-grids for the rotor blades rotate through the fixed OB Cartesian grid system. Overflow is coupled in a loosely manner with the helicopter comprehensive code CAMRAD II.[9] The CFD provides high-fidelity, nonlinear aerodynamics that replace

the comprehensive lifting line aerodynamic analysis from CAMRAD II. The comprehensive code performs the structural dynamics and trim calculations and gives the information to Overflow. The loose coupling allows for a modular approach and communication through input/output. The coupling methodology has been implemented following the approach of Potsdam *et al.*[10]

The numerical approach and the coupling process are described below.

A. Overset Grid Generation

The overset grid generation process using CGT can be divided into the following steps: geometry processing, surface grid generation, volume grid generation, and domain connectivity.[8]

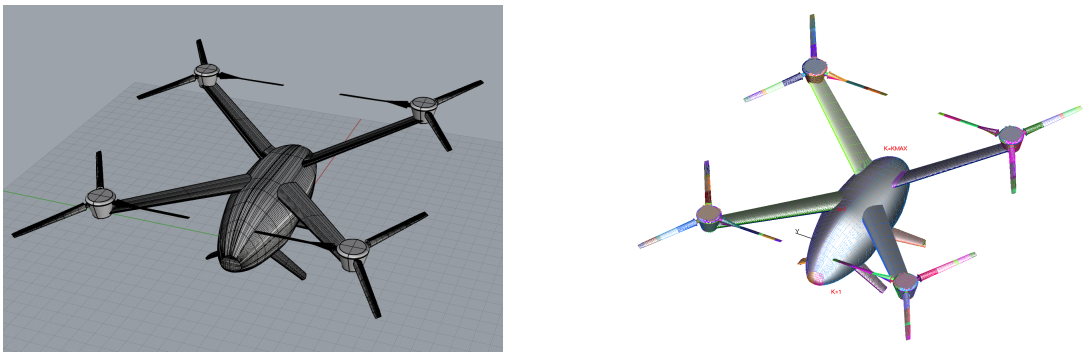

(a) CAD geometry.

(b) EGADS surface grids.

Figure 2: The quadrotor air taxi. The image on the left shows the CAD geometry, the image on the right shows the structured untrimmed patches obtained from the CAD geometry using EGADS. The patches are used as reference surfaces to generate the overset surface grids.

The geometry is usually obtained from a Computer Aided Design (CAD) model. Figure 2a shows the CAD model of the quadcopter vehicle. The Boundary Representation (BRep) is an object that holds both the topological entities and the geometric components.[11] In this work, a pre-processing step converts the analytical BRep solid from a STEP or IGES file into discrete representations for the BRep faces and edges. Access to the model topology and entities is accomplished through EGADS (the Engineering Geometry Aerospace Design System) API which is a foundational component of the Engineering Sketch Pad.[11] With the *egads2srf* tool, discrete representations are generated from each solid. Figure 2b shows the structured surface grid file obtained using EGADS. This grid file contains an untrimmed structured patch for each face based on tessellation of the face parameter space. Another file obtained with *egads2srf* is a curve grid file containing tessellated edges. The curve grid file and the structured grid file from EGADS are then used as an input for the overset surface grid generation step.

Overset structured surface meshes are typically created using a combination of algebraic or hyperbolic methods, depending on the number of initial curves on each surface domain. The generation of surface grids is the step that requires the most manual effort and experience from the user. Figure 3 shows the overset surface grids for the quadrotor complete vehicle. The complete vehicle consists of the rotors, hubs, hub supports, wings and main airframe. The landing gear has not been modeled in this work, and is left for future analysis.

With sufficient overlap between surface grids, the volume grids can be created easily with hyperbolic marching methods out to a fixed distance from the surface. Such methods provide orthogonal grids with tight clustering characteristics at the wall, which is essential for accurately capturing the boundary layer in viscous flow computations. The distance is chosen such that the outer boundaries of the NB volume grids are well clear off the boundary layer. The NB grids are then embedded inside OB Cartesian grids that extend to the far field. Figure 4a shows the Near-Body grids for the quadcopter with rotors, in Figure 4b the NB and the OB Cartesian grids are shown.

Off-Body Cartesian grids with uniform spacing surround the NB grids to resolve the wake region of interest. Coarser Cartesian grids efficiently expand the grid system to the far field, where each successive Cartesian grid is twice as coarse as its previous neighbor. The far field boundary is 20 rotor radii away from

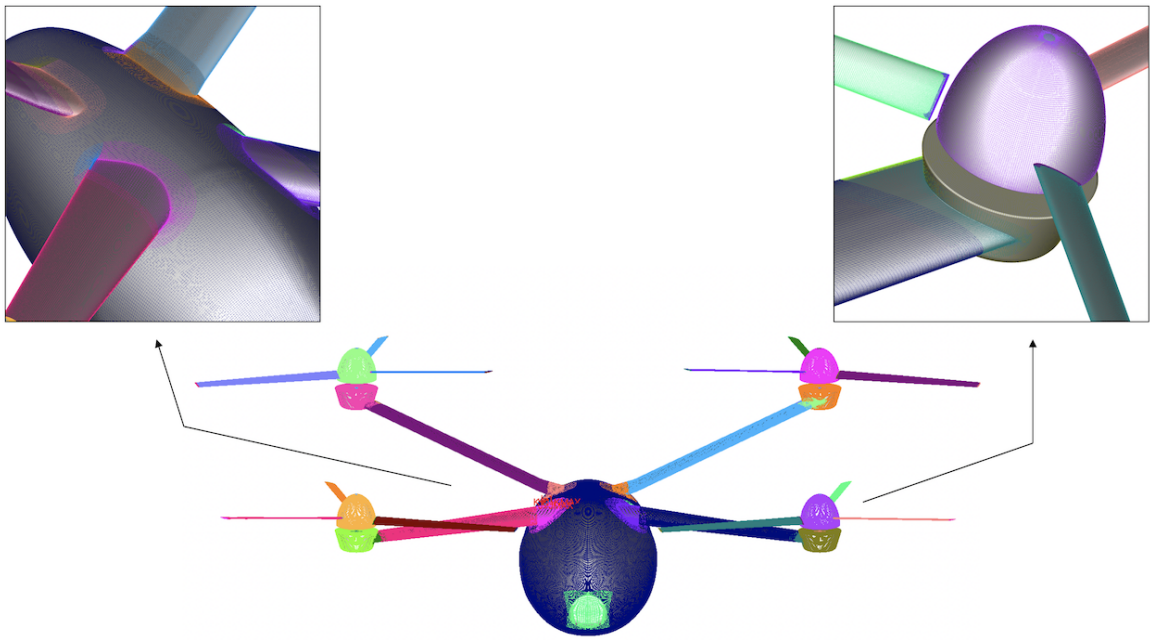

Figure 3: Quadrotor overset surface grids. The top left image shows in detail the collar grids for the junctions of the wings with the fuselage. The top right image illustrates a close-up view of the hub, hub support, wing-hub support junction, and blade root sections. The central image shows the front view of the quadcopter vehicle.

the center of the vehicle in all directions. The resolved wake region has a uniform grid spacing of 10% of the tip chord length c_{tip}.

The rotor geometry information from Table 1 has been used to generate the blade grids. The profiles used to build the blade are 10.6% thick modern airfoils from $r = 0$ to $r = 0.85R$, and 9% thick modern airfoils from $r = 0.95R$ to the tipf $r = R$. The transition between the two different airfoil sections is smooth (linear interpolation with the radial stations). The blade is tapered near the tip. Figure 5 shows in detail the quadrotor vehicle blade grids. Surface grid resolution on the rotor blades is clustered in the chordwise direction near the airfoils leading and trailing edges to accurately resolve large pressure gradients. Subsequently, the spanwise resolution is clustered near the root and the tip. The normal grid spacing of all grids at the walls maintains $y^+ \leq 1$.

Table 1: Quadrotor rotor geometry properties.

Number of rotors	4
Number of blades/rotor	3
Radius, R	2.809 m
Linear twist	-12 deg
Root chord, c_{root}	0.217 m
Tip chord, c_{tip}	0.176 m
Rotor solidity, σ	0.0647
Nominal tip speed, V_{tip}	167.6 m/s

The multi-rotor system consists of four rotors, each rotor made up of three blades. The right front rotor rotates counter-clockwise (CCW), the left front rotor rotates clockwise (CW), the right rear rotor rotates CW and the left rear rotor rotates CCW. Therefore the advancing blade is outboard for the front rotors, and inboard for the rear rotors. The rotor grids without airframe are shown in Figure 6. A -3^o alpha shaft angle is included for all the rotors. The locations of each rotor are summarized in Table 2. Johnson and

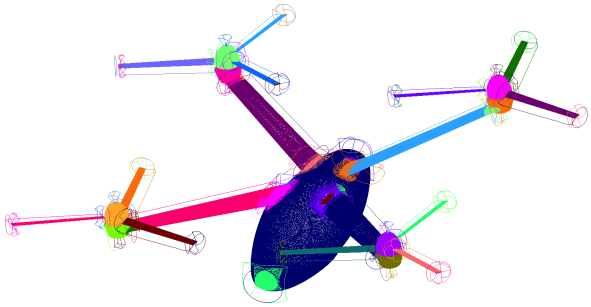

(a) NB volume grids, oblique view.

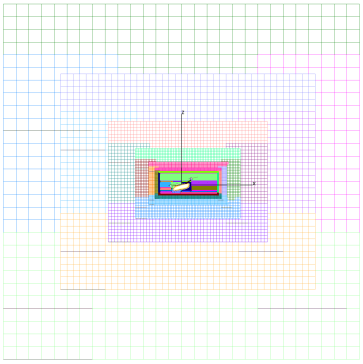

(b) NB+OB volume grids, side view.

Figure 4: Quadcopter overset volume grids. Figure (a) shows the NB volume grids of the quadcopter vehicle. Figure (b) shows the NB and OB volume grids.

Silva[6] obtained this final configuration of the quadcopter using MDAO tools, for which the power required to cruise is reduced by decreasing the interferences of the wakes of the front rotors on the rear rotors. In addition, "moving the aircraft center of gravity forward of the mid-point between the rotors, so the front and the rear rotors trim closer to the same C_T/σ at cruise speed, further reduces the power", they explained.

The design of the quadcopter has also been based on the findings from Ventura Diaz *et al.*,[3,4] where the rear rotors have a vertical separation from the front rotors in order to reduce rotor-rotor interactions in forward flight, by reducing the influence of the wakes from the front rotors on the rear rotors.

Table 2: Rotor placement of quadcopter vehicle.

Rotor Number	Rotation	x	y	z
Rotor 1	CCW	$-1.35R$	$1.35R$	$0.25R$
Rotor 2	CW	$-1.35R$	$-1.35R$	$0.25R$
Rotor 3	CW	$1.35R$	$1.35R$	$0.6R$
Rotor 4	CCW	$1.35R$	$-1.35R$	$0.6R$

Figure 7 shows the front view of the quadrotor rotors-only complete grid system, including the NB and OB volume grids. The total number of points reaches 311 million grid points, when using $10\%c_{tip}$ as the resolution of the first L1-box.

By using a trimmed approach, the domain connectivity step is robust and highly automated: hole cutting is required between components and with the OB Cartesian grids. In this study, the X-ray hole cutting method is used. An X-ray object is created for every component in the geometry (i.e. the blades, the hubs, the fuselage, the wings, etc.). The user has to supply the list of meshes that each X-ray object is allowed to cut, and an offset distance with which to grow each hole away from the body. The hole cutting process is performed at each time step within the flow solver, allowing for the rotation of the blades relative to the fixed components.

The number of grids and grid points for the configurations studied is presented in Table 3.

Table 3: NB and OB grid features of all configurations studied.

Configuration	NB grids	NB grid points	NB+OB grid points
Only-rotors	48	57×10^6	311×10^6
Complete vehicle	92	113×10^6	472×10^6

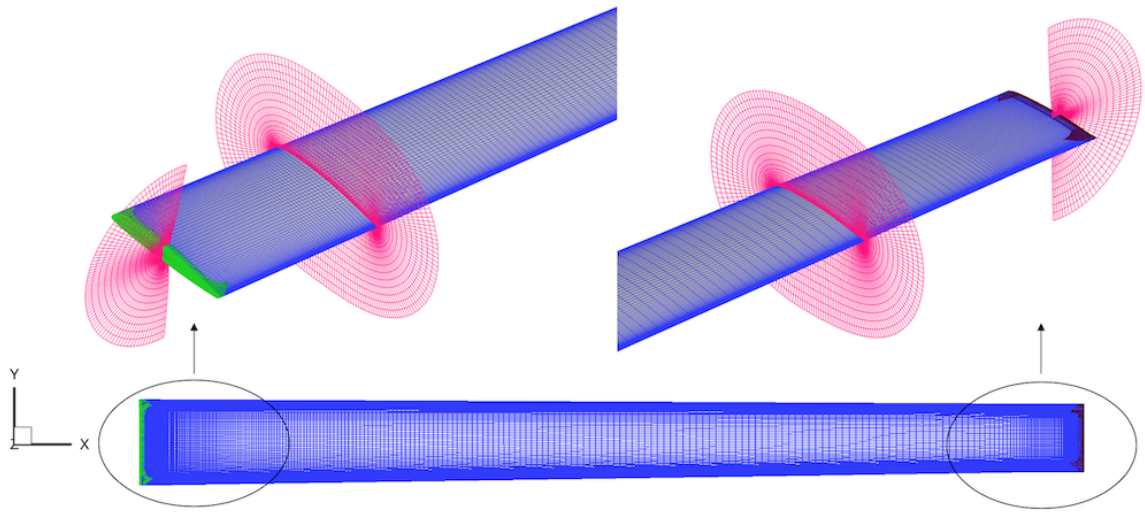

Figure 5: Blade overset grids for the quadrotor urban air taxi. The NB root and tip grids are shown in detail. Cap grids are used for the root (green) and tip (maroon), O-grids are used for the blade (blue). Slices of the volume grids are shown in magenta. There is clustering near the leading edge, trailing edge, blade tip and blade root, in order to solve the large pressure gradients near these regions.

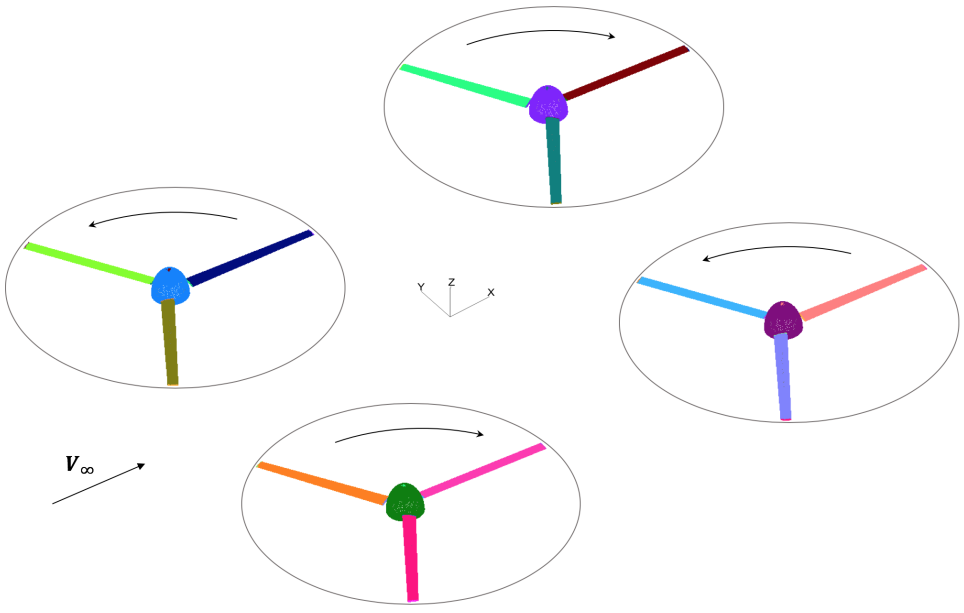

Figure 6: Quadrotor rotors-only overset surface grids. The image illustrates the direction of rotation of each individual rotor.

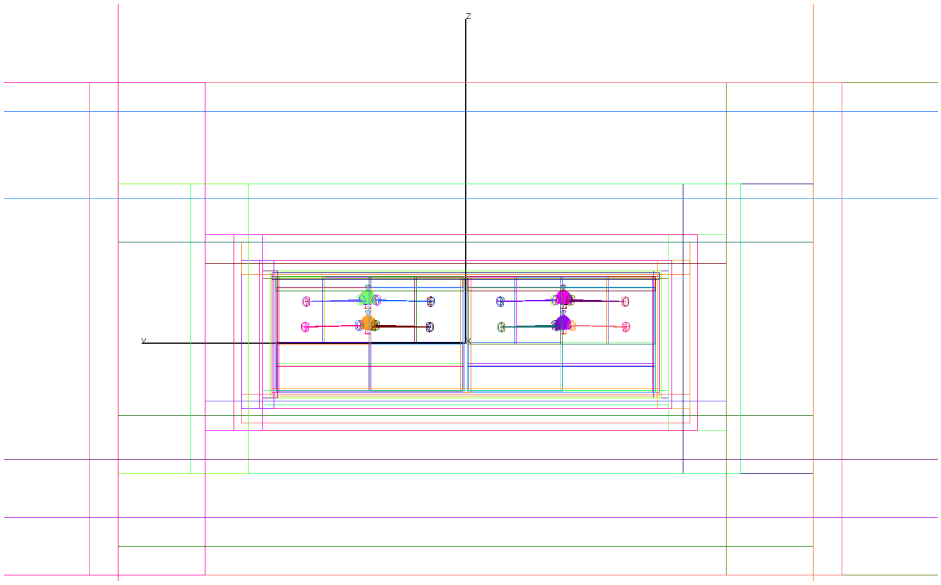

Figure 7: Front view of the quadrotor rotors-only grid system.

B. High-Order Accurate Navier-Stokes Solver

The Navier-Stokes equations can be solved using finite differences with a variety of numerical algorithms and turbulence models. The time dependent Reynolds-Averaged Navier-Stokes (RANS) equations are solved in strong conservation form:

$$\frac{\partial \boldsymbol{q}}{\partial t} + \frac{\partial(\boldsymbol{F} - \boldsymbol{F}_{\mathrm{v}})}{\partial x} + \frac{\partial(\boldsymbol{G} - \boldsymbol{G}_{\mathrm{v}})}{\partial y} + \frac{\partial(\boldsymbol{H} - \boldsymbol{H}_{\mathrm{v}})}{\partial z} = 0, \tag{1}$$

being $\boldsymbol{q} = [\rho, \rho u, \rho v, \rho w, e]^{\intercal}$ the vector of conserved variables; $\boldsymbol{F}$, $\boldsymbol{G}$ and $\boldsymbol{H}$ the inviscid flux vectors; and $\boldsymbol{F}_{\mathrm{v}}$, $\boldsymbol{G}_{\mathrm{v}}$ and $\boldsymbol{H}_{\mathrm{v}}$ the viscous flux vectors.

In this study, the diagonal central difference algorithm is used with the 4^{th}-order accurate spatial differencing option with matrix dissipation or 5^{th}-order accurate spatial differencing option with scalar dissipation. The physical time step corresponds to 0.25 degree rotor rotation, together with up to 50 dual-time sub-iterations for a 2.5 to 3.0 orders of magnitude drop in sub-iteration residual. The numerical approach and time step were previously validated for various rotor flows.[12–14] In order to reduce the computation time required for a converged solution, the first 1440 steps employ a time step equivalent to 2.5 degree per time step, yielding 10 rotor revolutions. The time step is then reduced to the equivalent of 0.25 degree per time step, for which 1440 steps correspond to one rotor revolution.

C. Hybrid Turbulence Modeling

The Overflow code has a choice of algebraic, one-equation, and two-equation turbulence models, including hybrid Reynolds-Averaged Navier-Stokes / Large Eddy Simulation (RANS/LES) models that close the RANS equations. In this study, the one equation Spalart-Allmaras[15] turbulence model is used primarily within the boundary layer.

The intent of the Detached Eddy Simulation (DES) model[15] is to be in RANS mode throughout the boundary layer, where the turbulent scales can be very small and need to be modeled, and in LES mode outside the boundary layer where the largest turbulent scales are grid-resolved. In this way, DES is a RANS/LES hybrid approach that mitigates the problem of artificially large eddy viscosity. The turbulence length scale d is replaced by $\overline{d}$, where $\overline{d}$ is the minimum of the distance from the wall, d, and the local grid spacing times a coefficient.

The DES approach assumes that the wall-parallel grid spacing $\Delta_{\parallel}$ exceeds the thickness of the boundary layer δ so that the RANS model remains active near solid surfaces. If the wall-parallel grid spacing is smaller than the boundary layer thickness, $\Delta_{\parallel} < \delta$ then the DES Reynolds stresses can become under-resolved within

the boundary layer; this may lead to non-physical results, including grid-induced separation. Using Delayed Detached Eddy Simulation (DDES),[16] the RANS mode is prolonged and is fully active within the boundary layer. The wall-parallel grid spacing used in this study does not violate the hybrid-LES validity condition; thus DES and DDES should give similar results. Nevertheless, all computations have been performed using the DDES model for both NB and OB grids.

D. Comprehensive Analysis

Structural dynamics and rotor trim for the coupled calculations are performed using the comprehensive rotorcraft analysis code CAMRAD II.[9] CAMRAD II is an aeromechanics analysis of rotorcraft that incorporates a combination of advanced technologies, including multibody dynamics, nonlinear finite elements, and rotorcraft aerodynamics. The trim task finds the equilibrium solution for a steady state operating condition, and produces the solution for performance, loads, and vibration. The aerodynamic model for the rotor blade is based on lifting-line theory, using two-dimensional airfoil characteristics and a vortex wake model. CAMRAD II has undergone extensive correlation with performance and loads measurements on rotorcraft.

E. Loose Coupling Overflow – CAMRAD II

A loose coupling approach between Overflow and CAMRAD II based on a trimmed periodic rotor solution is implemented. The comprehensive code provides the trim solution and blade motions. The high-fidelity CFD calculates the airloads. Figure 8 shows the flow diagram of the loose coupling strategy. In summary, the CFD airloads replace the comprehensive airloads while using lifting line aerodynamics to trim and computational structural dynamics to account for blade deformations.

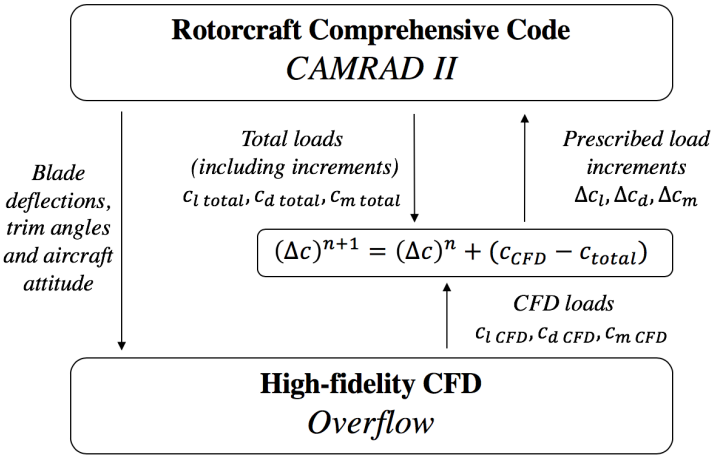

Figure 8: Flow diagram for CFD/Comprehensive Analysis loose coupling methodology.

The iterative loose coupling process is summarized next. The simulation is initialized with a comprehensive analysis resulting in a trimmed rotor solution obtained with lifting line aerodynamics. This analysis creates initial quarter chord motions as a function of the radius r and the azimuth ψ, for each rotor. In addition, the aircraft attitude is also obtained from CAMRAD II. The motions and aircraft pitch angle are given to the CFD. The CFD analysis accounts for the entire flow field, and therefore it only requires the structural motion. The CFD is run with the prescribed motions and angles, for two to three full rotor revolutions for the first coupling step. Overflow outputs the normal force N', pitching moment M', and chord force C' as a function of radius and azimuth.

Then, the aerodynamic force and moment coefficients increments (Δc) that are used in the comprehensive code at the next iteration $n+1$ are calculated. The increments are the difference between the CFD loads and the comprehensive lifting line solution required to trim from the previous step n, plus the load increments from the previous step:

$$(\Delta c)^{n+1} = (\Delta c)^n + (c_{CFD} - c_{total}) \tag{2}$$

For the initial step, the increments are the difference between CFD and the total loads from the 0^{th} run in CAMRAD II:

$$(\Delta c)^1 = (c_{CFD} - c_{total})$$

The sectional pitching moment M^2c_m, normal force M^2c_n and chord force M^2c_c coefficients are defined as:

$$M^2c_m = \frac{M'}{\frac{1}{2}\rho a^2 c^2} \tag{3}$$

$$M^2c_n = \frac{N'}{\frac{1}{2}\rho a^2 c} \tag{4}$$

$$M^2c_c = \frac{C'}{\frac{1}{2}\rho a^2 c} \tag{5}$$

With the new quarter chord motions of the retrimmed rotor and the new aircraft attitude, the CFD is rerun. The previous CFD flow solution is used as restart condition. The coupling is performed every half or quarter rotor revolution. The coupling solution is considered to be converged when collective and cyclic control angles and the CFD aerodynamic forces do not change between iterations. The CFD flow solution is usually converged after 10 to 20 rotor revolutions.

The coupling procedure is valid as long as the rotor loads are periodic. This approach is still good if there is some aperiodicity in the vortex wake, which is often the case in high-resolution turbulent simulations.

III. Results

NASA's quadrotor concept is simulated using the comprehensive rotorcraft code CAMRAD II and the high-fidelity CFD solver Overflow. CAMRAD II provides the trim solution and the rigid motion of the blades to Overflow. Overflow solves the Navier-Stokes flow equations with the rotor information. The loosely coupled methodology provides a more accurate strategy to calculate the rotor loads.

The overset grids described in the previous sections are used for the quadcopter air taxi concept. First, the "rotors-only" configuration, which consists of four three-bladed rotors and four hubs, is simulated in cruise and in hover. The airloads and wake geometries will be studied. The effect of the vertical separation on the power in cruise will be presented. Then, the complete vehicle will be examined.

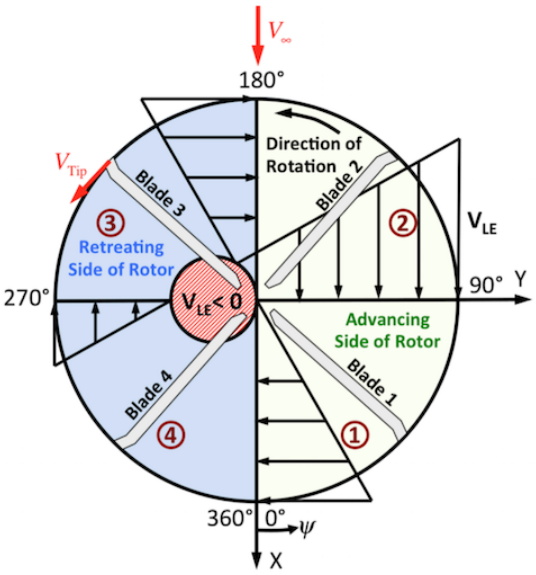

Figure 9: Edgewise forward flight flow conditions and parameters for a single CCW rotor.[17]

The main flow features and parameters used to analyze rotors in forward flight are presented in Figure 9, for a rotor rotating CCW. The blade is on the advancing side of the rotor disk when $0^o < \psi < 180^o$, and

between $180^o < \psi < 360^o$, the blade is on the retreating side. Near the root, on the retreating side, there exists a region of reversed flow. The locus of this region can be found where the in-plane component of the local flow velocity is equal to zero. That is:

$$0 = \Omega R(r + \mu \sin \psi)$$

which has the simple solution $r = -\mu \sin \psi$. Therefore, the reverse flow region on the rotor disk is a circle of diameter μ. With increasing advance ratios, the size of the region with reversed flow on the retreating side increases.

All simulations have been carried out with NASA's supercomputers Pleiades and Electra, located at the NASA Advanced Supercomputing (NAS) Division, utilizing from 1000 to 3000 processors on Broadwell and Electra nodes.

A. Quadcopter Rotors-Only Configuration in Cruise

First, the "rotors-only" configuration from Figure 6 will be simulated in cruise. The flight condition simulated is the best-range cruise, at $h = 5000$ ft and $T =$ ISA +20 ^{o}C, with an advance ratio of $\mu = 0.373$. Table 4 summarizes the flow conditions.

Table 5 shows the front rotors z_{front} and rear rotors z_{rear} vertical positions for each case analyzed. The baseline case is Case 4, with $z_{rear} = 0.6R$. It will be shown later that this case has the highest power reduction, while keeping a compact configuration.

Table 4: Best range cruise flow conditions for the quadrotor urban air taxi simulations.

h	5000 ft
T_∞	ISA +20^{o}C
V_∞	121.6 kts
N	499.7 rpm
M_{tip}	0.484
M_∞	0.181
μ	0.373
Re	$1.7 \cdot 10^6$

Table 5: Different rear rotor vertical positions analyzed for quadcopter "rotors-only" configuration.

Case number	z_{front}	z_{rear}
Case 1	$0.25R$	$0.25R$
Case 2	$0.25R$	$0.4R$
Case 3	$0.25R$	$0.5R$
Case 4	$0.25R$	$0.6R$

Table 6: Final angles for the quadcopter "rotors-only" configuration, in cruise conditions, with $z_{front} = 0.25R$ and $z_{rear} = 0.6R$.

Rotor number	β_0 [^{o}]	β_{1c} [^{o}]	β_{1s} [^{o}]	θ_0 [^{o}]
Rotor 1 (front-right)	2.46	-5.13	3.97	15.77
Rotor 2 (front-left)	2.44	-5.15	3.97	15.73
Rotor 3 (rear-right)	2.56	-5.41	4.26	16.49
Rotor 4 (rear-left)	2.58	-5.41	4.25	16.52

The Overflow - CAMRAD II coupling approach is considered converged when the delta airloads differences between one iteration to the next are very small. This is also reflected on the trim angles evolution. Figure 10 shows the coning angle β_0, the flapping angles β_{1c} and β_{1s}, and the collective pitch angle θ_0 for the four rotors, where rotor 1 is the front-right rotor, rotor 2 is the front-left rotor, rotor 3 is the rear-right rotor, and rotor 4 is the rear-left rotor. After approximately 12 iterations, the change in trim angles is relatively small, and thus the coupling approach can be considered to be converged.

The CAMRAD II model uses collective control for trimming the rotorcraft, with the four rotors rotating at the same rotational speed, shown in Table 4. The thrust of the rear rotors relative to the front rotors increases as the forward flight speed increases. Therefore, the collective angle is found to be higher for the rear rotors than for the front rotors in edgewise flight. Table 6 shows the final coning, flapping and collective angles of each rotor. There is no cyclic control for this air taxi concept, and thus $\theta_{1c} = \theta_{1s} = 0^o$. The collective trim angle is approximately 0.8^o higher for the rear rotors.

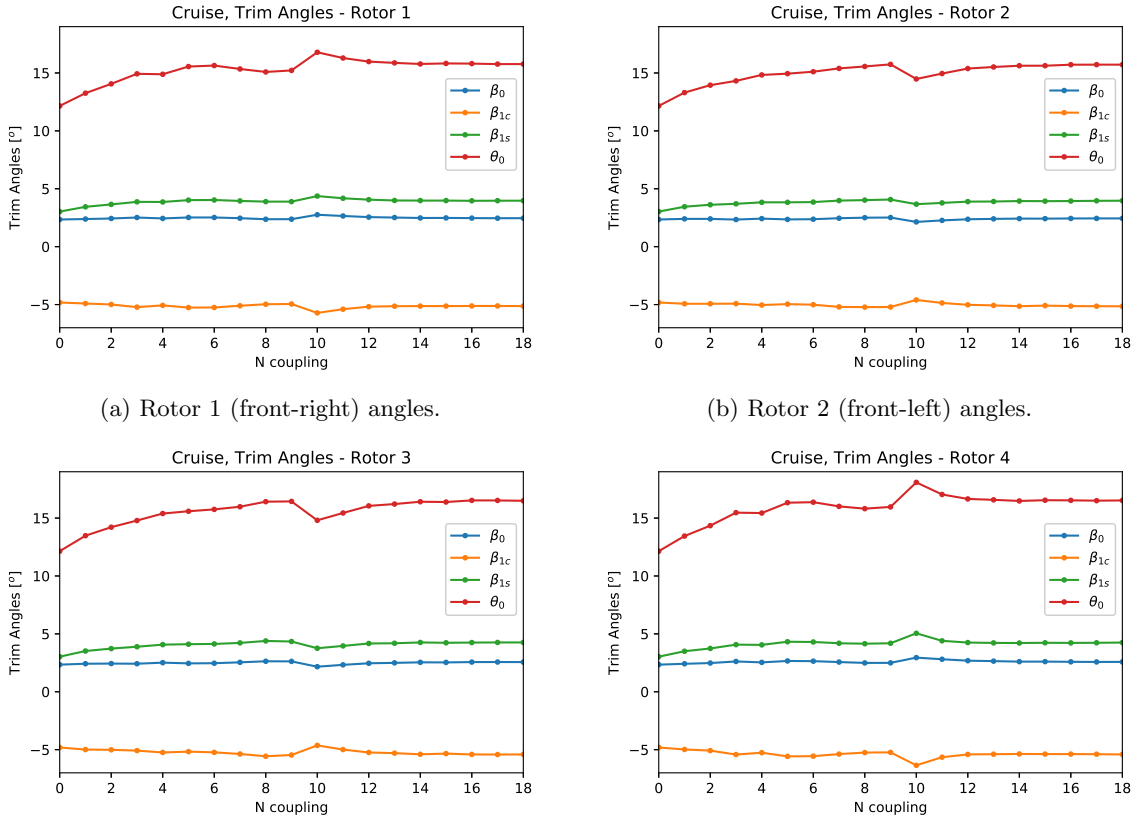

(a) Rotor 1 (front-right) angles.

(b) Rotor 2 (front-left) angles.

(c) Rotor 3 (rear-right) trim angles.

(d) Rotor 4 (rear-left) trim angles.

Figure 10: Quadcopter "rotors-only" flapping and collective angles evolution with the number of loose-coupling iterations, in cruise.

Airloads

The airloads on the rotor disks are presented in Figure 11 for the configuration with $z_{rear} = 0.6R$. The normal force coefficient $M^2 c_n$, chord force coefficient $M^2 c_c$ and pitch moment coefficient $M^2 c_m$, are illustrated, where M is the local Mach number. Consistent symmetry can be found between the right and left rotors.

In the normal force coefficient images (Figure 11a), the reversed flow region can be observed as where c_n is negative, see the blue zones on the retreating side near the root. In order to have a total pitch moment of zero on the disk, the flapping motion of the blades causes the normal force to be low near the tip at the advancing side of the rotor disk. As a consequence, the vortices on the advancing side are weak. This will be later observed on the images of the rotor wake. Highest local lift values are produced at the front ($\psi = 180^o$)

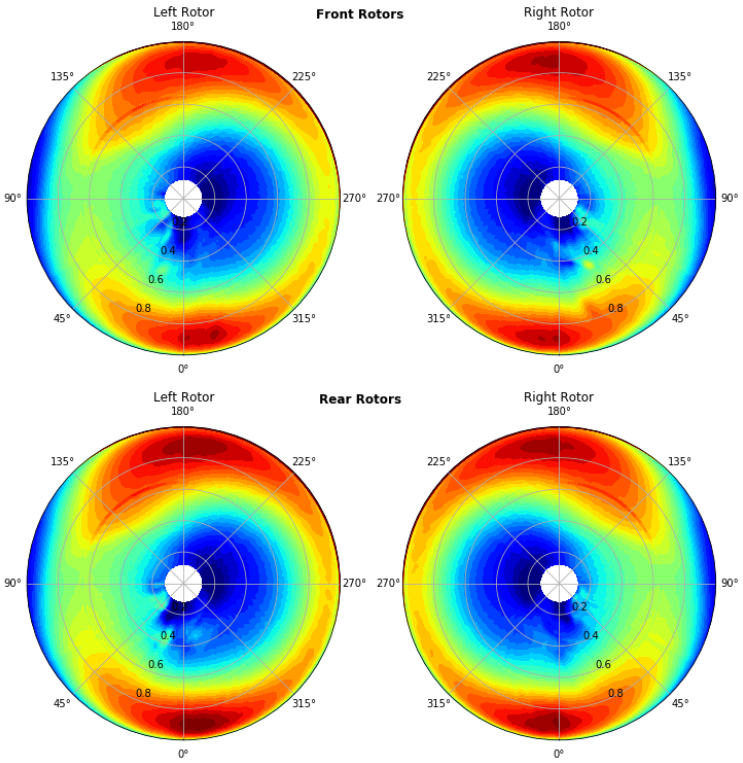

(a) Normal force coefficient $M^2 c_n$.

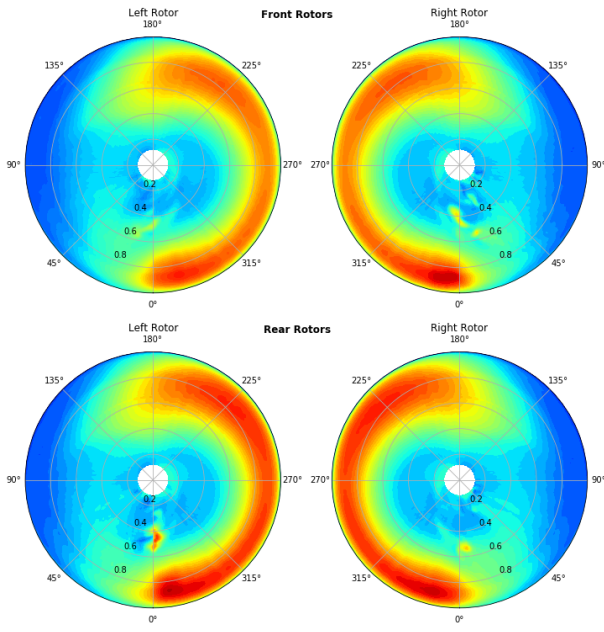

(b) Chord force coefficient $M^2 c_c$.

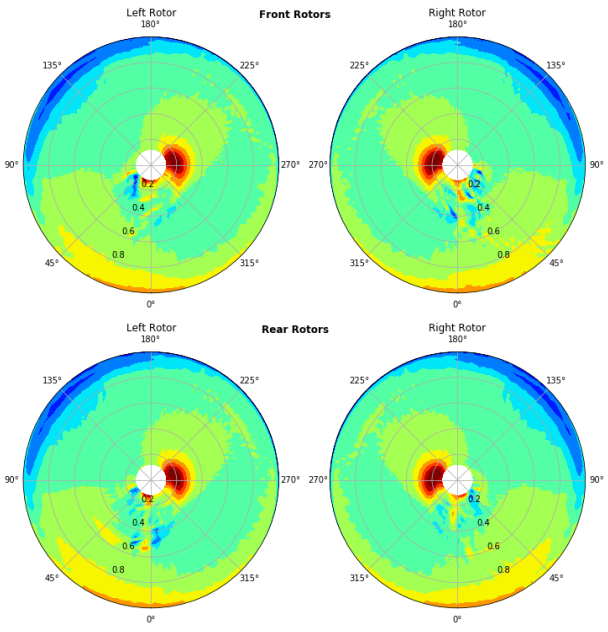

(c) Pitch moment coefficient $M^2 c_m$.

Figure 11: Normal force $M^2 c_n$, chord force $M^2 c_c$ and pitch moment $M^2 c_m$ coefficients on the rotor disk in cruise, for the four rotors. The rotor disks are seen from a plane above the quad-rotor: the top-right disk corresponds to the front-right rotor, the top-left disk represents the front-left rotor, the bottom-right disk is the rear-right rotor, and the bottom-left disk is the rear-left rotor.

and at the back ($\psi = 0^o$) of the rotor disk.

The local chord coefficient, is shown in Figure 11b. The aerodynamic chordwise coefficient is positive in the negative local drag direction. Darker red regions are observed for the rear rotors at the inboard locations, meaning that the local chord force is higher in those regions.

Figure 11c illustrates the local pitch moment coefficient c_m. Negative pitch moments are found near the tip on the advancing side, and high positive pitch moments are located near the root on the reversed flow region.

Wake Geometry

The wake geometry is presented in this section. By visualizing the vortex wake, rotor-rotor interactions can be observed.

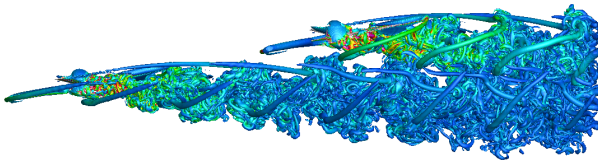

(a) Q-criterion iso-surfaces, $z_{rear} = 0.25R$

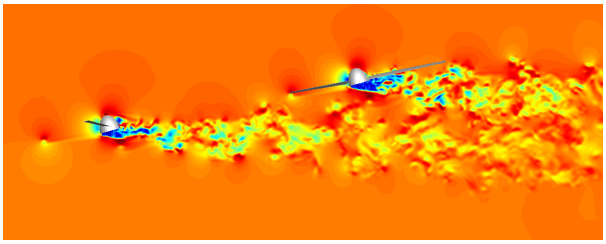

(b) Velocity magnitude contour, $z_{rear} = 0.25R$

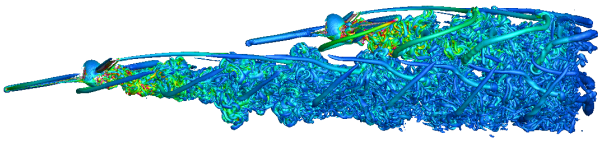

(c) Q-criterion iso-surfaces, $z_{rear} = 0.4R$

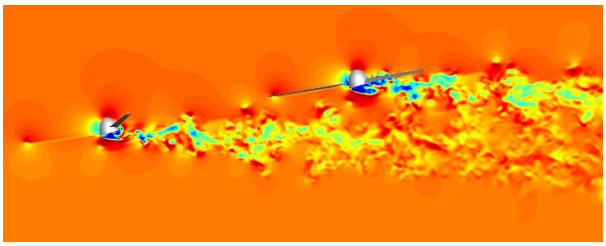

(d) Velocity magnitude contour, $z_{rear} = 0.4R$

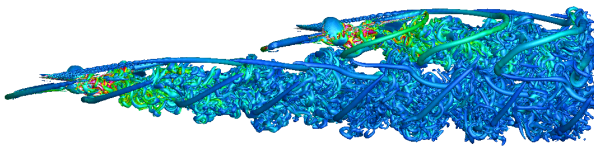

(e) Q-criterion iso-surfaces, $z_{rear} = 0.5R$

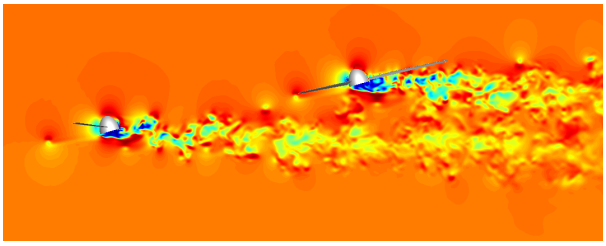

(f) Velocity magnitude contour, $z_{rear} = 0.5R$

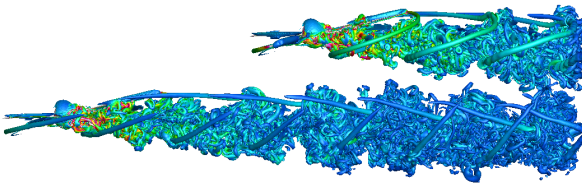

(g) Q-criterion iso-surfaces, $z_{rear} = 0.6R$

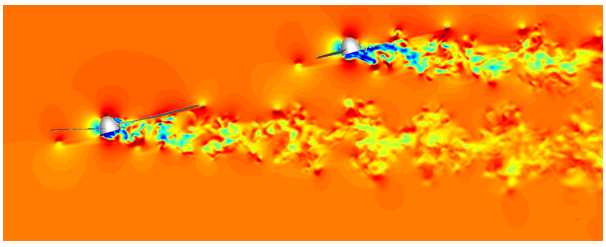

(h) Velocity magnitude contour, $z_{rear} = 0.6R$

Figure 12: Vortex wake of the quadrotor "rotors-only" configuration in cruise conditions, for different rear rotor vertical placements z_{rear}, side views. The rotor-rotors interactions are stronger when the distance between rotors is smaller. The iso-surfaces are colored by the vorticity magnitude.

The rotor wakes for the four cases from Table 2 are shown in Figures 12 and 13. The images on the

left from Figure 12 show the Q-criterion vorticity iso-surfaces and the images on the right show the velocity magnitude. With this side-view, it can be observed the influence of the vortex wake of the front rotors on the rear rotors.

Figure 13 shows an oblique view of the Q-critertion vorticity iso-surfaces. The trimmed blades produce relatively weak vortices on the advancing side and strong vortices on the retreating side. In addition, the blade-vortex interactions (BVI) occur on the advancing side near the root, and on the retreating side near the root. Then, vortices travel downstream and may intersect the rear rotors. By increasing the vertical separation, the wakes from the front rotors affect less the rear rotors.

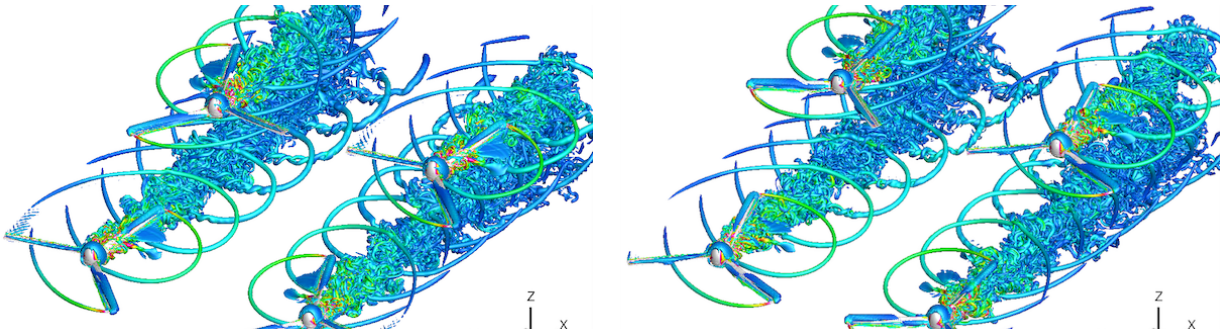

(a) Q-criterion iso-surfaces, $z_{rear} = 0.25R$ (b) Q-criterion iso-surfaces, $z_{rear} = 0.6R$

Figure 13: Vortex wake of the quadrotor "rotors-only" configuration in cruise conditions, for two different rear rotor vertical placements z_{rear}, oblique views. The iso-surfaces are colored by the vorticity magnitude.

Power Reduction

Since the aircraft is being trimmed to the same flight condition for all the cases using the CAMRAD II rotorcraft comprehensive code, the rotors trim to the same total thrust. However, as the vertical separation is increased, the rotor-rotor interactions decrease, and so does the power required to keep a steady cruise flight condition. The power required to fly in cruise is the lowest for the case with the highest vertical separation. Increasing the vertical separation would reduce the power further, however, a realistic and compact configuration has to be designed.[a]

Figure 14 illustrates the power reduction as the vertical separation $z_{rear} - z_{front}$ increases. The reference power is the rotor power calculated for case 1, where $z_{rear} - z_{front} = 0$. An 8% decrease in the total rotor power in cruise is found for when the rear rotors are located at $z_{rear} = 0.6R$.

The rotors with $z_{rear} = 0.6R$ will be used for the remaining of this work.

Rotor-rotor interactions have a significant impact on performance, noise, and vibrations. The interactions strongly depend on the positioning of the rotors. Elevating the rear rotors above the front rotors reduces the rotor-rotor interactions by reducing the interferences of the wakes.

B. Quadcopter Rotors-Only Configuration in Hover

The "rotors-only" configuration with $z_{front} = 0.25R$ and $z_{rear} = 0.6R$ has been simulated in hover too. In hover, the freestream velocity is $V_\infty = 0$. Since the front rotors are placed lower than the rear rotors with a -3^o alpha shaft angle, they will trim to a higher collective in order to compensate for the difference in vertical position.

Figure 15 illustrates the evolution of the flapping and collective angles for the four rotors in hover conditions. Table 7 shows the final angles for the four rotors. The collective is approximately 1.5^o higher for the front rotors. The magnitude of coning and flapping angles is similar between the front and rear rotors, but the signs of lateral and longitudinal flapping are reversed. Lateral and longitudinal flapping angles are small, but their presence prevents the flow on the rotor disk to be axisymmetric, as it would be expected for an isolated rotor in hover.

[a]In addition, an extreme separation would also increase the total weight of the vehicle, which would increase the power, parameter that has not been included in this study.

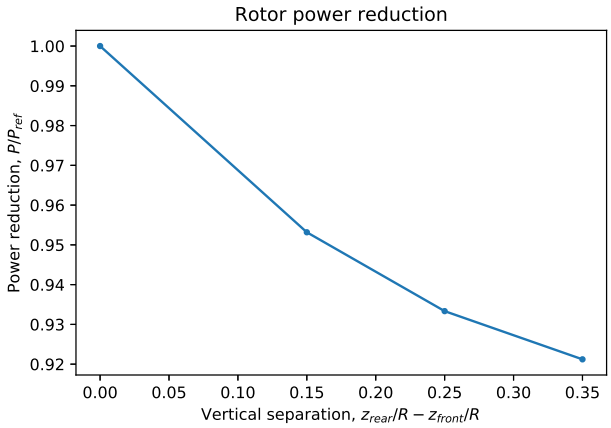

Figure 14: Total rotor power P/P_{ref} as a function of the vertical separation $z_{rear}/R - z_{front}/R$. The reference power is calculated for the case without vertical separation, $z_{front} = z_{rear} = 0.25R$.

Table 7: Final angles for the quadcopter "rotors-only" configuration, in hover conditions, with $z_{front} = 0.25R$ and $z_{rear} = 0.6R$.

Rotor number	β_0 [^{o}]	β_{1c} [^{o}]	β_{1s} [^{o}]	θ_0 [^{o}]
Rotor 1 (front-right)	2.74	-0.39	0.21	12.72
Rotor 2 (front-left)	2.73	-0.38	0.22	12.70
Rotor 3 (rear-right)	2.38	0.48	-0.29	11.36
Rotor 4 (rear-left)	2.38	0.48	-0.3	11.37

Airloads

The airloads on the rotor disks are presented in Figure 16. The normal force coefficient M^2c_n, chord force coefficient M^2c_c and pitch moment coefficient M^2c_m, are illustrated. An isolated rotor in hover flight experiences an axisymmetric flow. However, in the case of the quadcopter, rotor-rotor interactions are present, the incoming flow to the rotors is not axisymmetric, and thus the rotor airloads are not axisymmetric neither. There is small flapping present on the rotor disk, as shown in Table 7. This can be clearly observed in Figures 16a and 16b. Lateral and longitudinal flapping changes sign between the front and rear rotors, changing the quadrant where the local normal coefficient decreases. Apart from this small dissymetry in the flow seen more clearly near the tip regions, local lift increases gradually with the radial position, as expected for a hovering rotor. The local pitch moment coefficient is almost uniform throughout the rotor disk, as seen in Figure 16c.

For the same total lift, the required power to hover is higher relative to edgewise flight for low advancing ratios, due to the lower flow through the disk. However, as advancing ratio increases, power in edgewise flight increases as well as the parasite power increases.[6]

Wake Geometry

The wake geometry of the quadrotor without airframe is illustrated in Figure 17a. BVI can be clearly observed in this case. Rotor-rotor interactions deflect the flow, and some turbulent structures appear in the central region.

Figure 17 shows a view from the top of the four rotors, with a slice below the front rotors ($z_{cut} = 0$). In these image in can clearly be observed the effect of the rotor-rotor interactions on the flowfield, as they deflect the velocity field breaking the axi-symmetry characteristic of isolated rotors in hover. These images reflect that rotor-rotor interactions are an important factor to consider in order to analyze the airloads and performance of multi-rotor vehicles, as they can change the flowfield considerably.

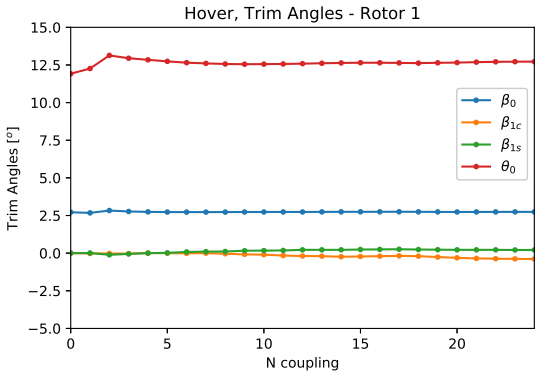

(a) Rotor 1 (front-right) angles.

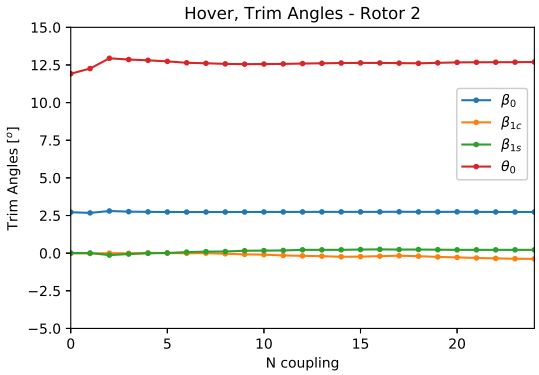

(b) Rotor 2 (front-left) angles.

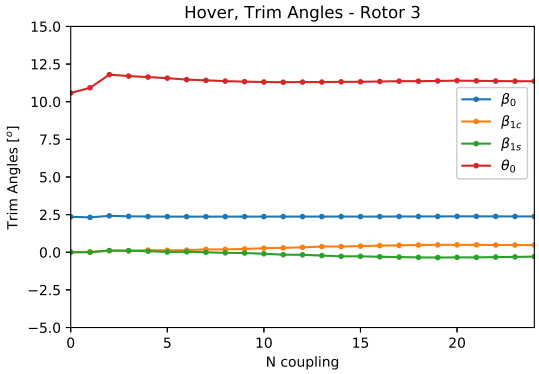

(c) Rotor 3 (rear-right) trim angles.

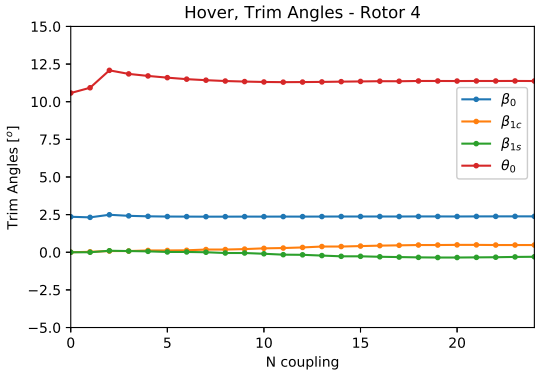

(d) Rotor 4 (rear-left) trim angles.

Figure 15: Quadcopter "rotors-only" flapping and collective angles evolution with the number of loose-coupling iterations, in hover.

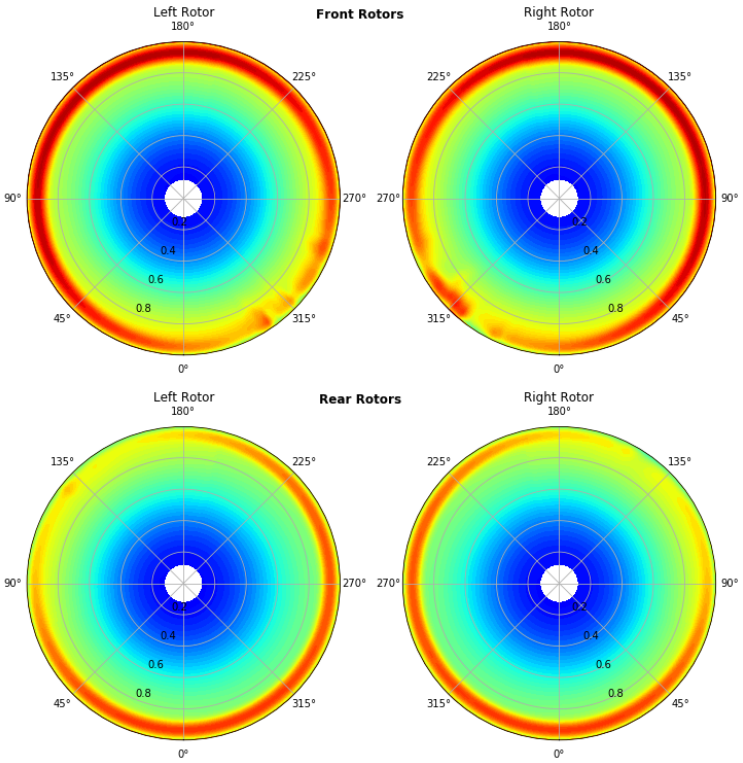

(a) Normal force coefficient $M^2 c_n$.

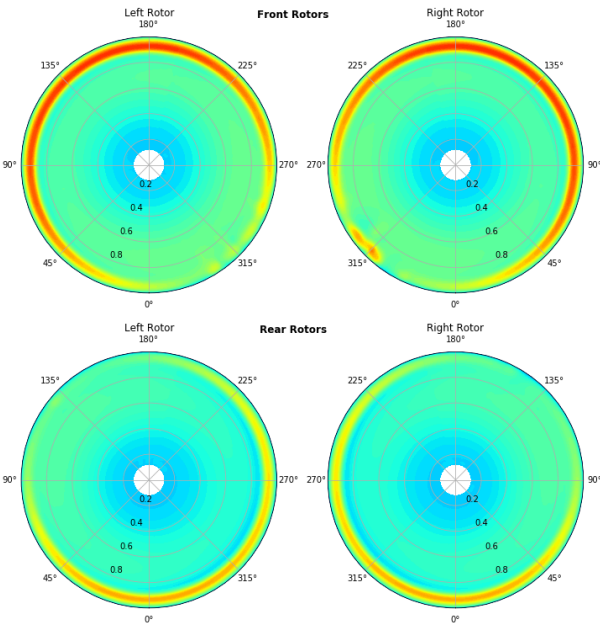

(b) Chord force coefficient $M^2 c_c$.

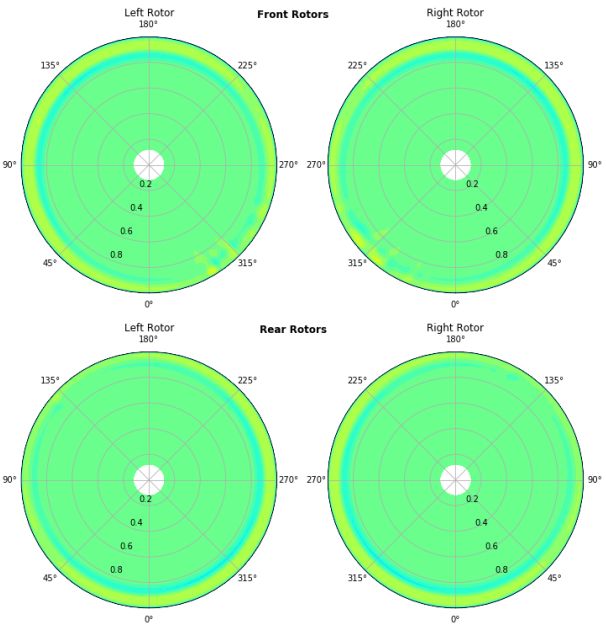

(c) Pitch moment coefficient $M^2 c_m$.

Figure 16: Normal force $M^2 c_n$, chord force $M^2 c_c$ and pitch moment $M^2 c_m$ coefficients on the rotor disk in hover, for the four rotors. The rotor disks are seen from a plane above the quad-rotor: the top-right disk corresponds to the front-right rotor, the top-left disk represents the front-left rotor, the bottom-right disk is the rear-right rotor, and the bottom-left disk is the rear-left rotor.

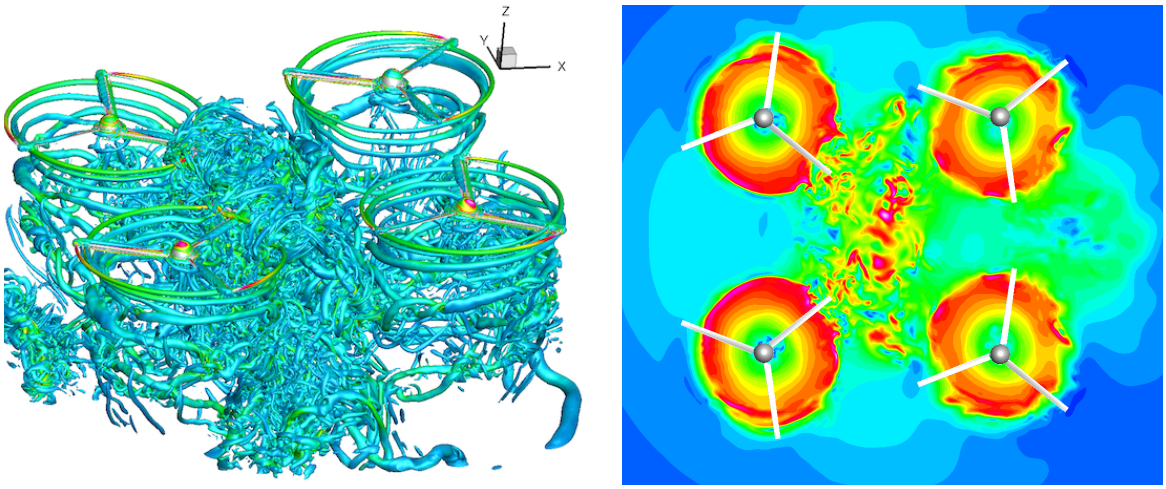

(a) Q-criterion vorticity iso-surfaces.

(b) Velocity magnitude contour.

Figure 17: Quadrotor without airframe in hover Figure (a) shows the vortex wake of the quadrotor visualized by the Q-criterion vorticity iso-surfaces, colored with the vorticity magnitude. Figure (b) shows the top view of the velocity contours at a cut plane $z_{cut} = 0$. Rotor-rotor interactions are an important factor to consider in order to analyze the airloads and performance of multi-rotor vehicles.

C. Quadrotor Complete Vehicle Configuration

This section covers a short analysis of the complete vehicle, recall Figure 3 for the overset surface grids of the complete configuration. The geometry consists of rotors, hubs, hub supports, wings, and airframe. The number of grid points is increased considerably, in addition to the complexity of the flow.

The notably higher number of grid points for this configuration increased the computer time to obtain a final flow solution.

The final design of the quadcopter has the rotor placements from Table 2. Figure 18 shows the vortices with Q-criterion iso-surfaces, colored with the vorticity magnitude (Figure 18a). The velocity contours at the center of the vehicle ($y = 0$) are shown in Figure 18b. It can be observed that the flow remains attached to the airframe, showing a remarkably good design of the airframe for this flight condition. Figure 18c shows the velocity contours at a rotor plane ($-y = 1.35R$). Notice similar flow features than to the case without airframe (Figure 12h).

A fine visualization of the flowfield can be found in Figure 19. The vortices are visualized with the Q-criterion, colored with the vorticity magnitude, and the background shows the pressure coefficient. Pressure fluctuations arise from the BVI, rotor-rotor interactions, rotor interactions with other components, etc., producing a complex pattern that propagates into the farfield. The high grid resolution allows to capture these pressure fluctuations. Future work will include a complete acoustic analysis of NASA's UAM vehicles.

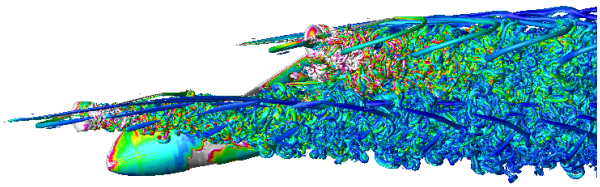

(a) Q-criterion vorticity iso-surfaces.

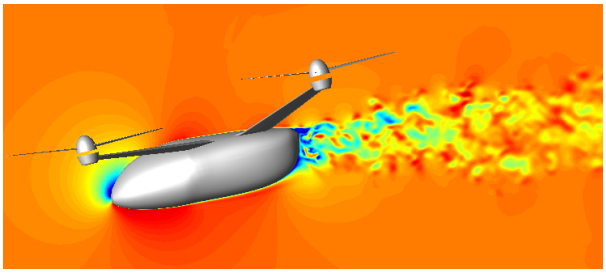

(b) Velocity magnitude contour.

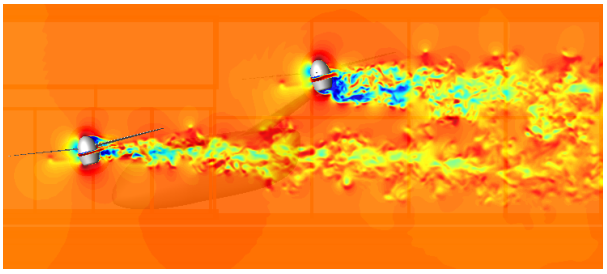

(c) Velocity magnitude contour.

Figure 18: Complete quadcopter vehicle in cruise, side views. Figure (a) shows the vortex wake of the quadrotor visualized by the Q-criterion vorticity iso-surfaces, colored with the vorticity magnitude. Figure (b) shows the velocity contours at a cut plane $y_{cut} = 0$. Figure (c) shows the velocity contours at a cut plane $y_{cut} = -1.35R$.

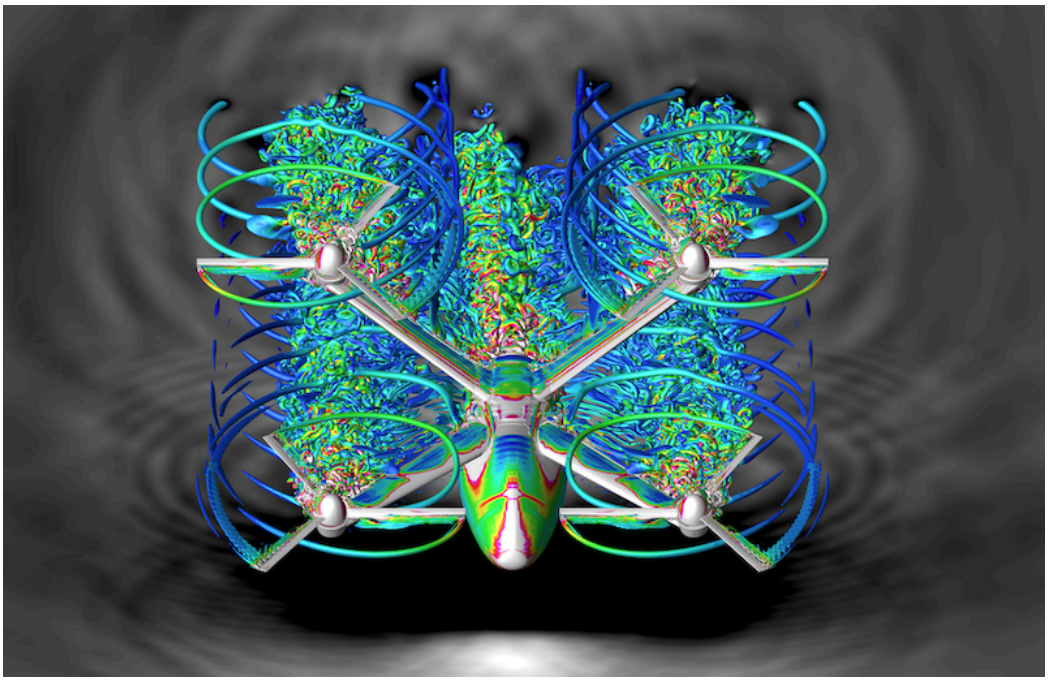

Figure 19: Visualization of the flow of NASA's six-passenger quadcopter concept for UAM, in edgewise flight (front-oblique view). The quadcopter vehicle design reduces rotor-rotor interactions between the front and rear rotors, while keeping an efficient and compact configuration. The background shows the pressure oscillations, where white is high and black is low. This image reveals the complexity of the flow for a multi-rotor configuration, where many rotors interact with each other and the different components.

IV. Summary

NASA's quadrotor air taxi concept has been simulated. A loosely coupled approach to simulate the flow of the quadrotor system in cruise conditions has been followed. The rotorcraft comprehensive code CAMRAD II and the overset finite-differences Navier-Stokes high-order accurate CFD solver Overflow have been coupled. CAMRAD II provides the blade motions and aircraft attitude to Overflow and Overflow accurately solves the flow, and then the aerodynamic loads obtained with Overflow are sent as an input to CAMRAD II, which recalculates the new trim solution and updates the blade motions and aircraft angles.

The airloads of the quadcopter have been studied, comparing the distributions between the front and rear rotors. The trimmed rotors showed weak vortices on the advancing side and strong vortices on the retreating side.

The effect of vertical separation on the power reduction for a trimmed aircraft has been assessed, finding that the power required to fly in forward flight decreases as the rotor-rotor interactions decrease, by increasing the vertical separation between the front and the rear rotors. The trim angles, airloads and wake geometry have been presented.

The hover flow condition has then been analyzed, showing the main flow characteristics of a quadrotor in hover. Again, the trim angles, airloads and wake geometries have been analyzed. Rotor-rotor interactions are also important in hover, and their effect has been evaluated.

To finish this work, the flow of the complete quadcopter has been presented. Future work will include a more extensive study of the complete vehicle.

NASA's quadcopter air taxi concept is one of the concept vehicles expected to focus and guide NASA's research activities in support of aircraft development for emerging aviation markets, in particular VTOL air taxi operations.

V. Acknowledgements

This work is supported by the Revolutionary Vertical Lift Technology (RVLT) Project (PM: Susan Gorton; PI: Brian Allan). The computations utilized the Pleiades and Electra supercomputers at the NASA Advanced Supercomputing Division. The authors would like to thank Wayne Johnson, Chris Silva, Brian Allan and Gloria Yamauchi, for helpful discussions.

References

[1]Ventura Diaz, P., Johnson, W., Ahmad, J., and Yoon, S., "The Side-by-side Urban Air Taxi Concept", AIAA Paper 2019-2828, The AIAA Aviation Forum 2019, Dallas, Texas, June 2019.

[2]Ventura Diaz, P., Caracuel Rubio, R., and Yoon, S., "Simulations of Ducted and Coaxial Rotors for Air Taxi Operations", AIAA Paper 2019-2825, The AIAA Aviation Forum 2019, Dallas, Texas, June 2019.

[3]Ventura Diaz, P. and Yoon, S., "High-Fidelity Computational Aerodynamics of Multi-Rotor Unmanned Aerial Vehicles", AIAA Paper 2018-1266, The AIAA SciTech Forum 2018, Kissimmee, Florida, January 2018.

[4]Ventura Diaz, P. and Yoon, S., "A Physics-Based Approach to Urban Air Mobility", The European Rotorcraft Forum, Paper 18, Delft, The Netherlands, September 2018.

[5]Yoon, S., Ventura Diaz, P., Boyd, D. D., Chan, W. M., and Theodore, C. R.,"Computational Aerodynamic Modeling of Small Quadcopter Vehicles", AHS Paper 73-2017-0015, The 73rd Annual AHS International Forum & Technology Display, Fort Worth, Texas, May 2017.

[6]Johnson, W. and Silva, C.,"Observations from Exploration of VTOL Urban Air Mobility Designs", The Asian/Australian Rotorcraft Forum, Jeju Island, Korea, October 30 – November 1, 2018.

[7]Pulliam, T. H., "High Order Accurate Finite-Difference Methods: as seen in OVERFLOW", AIAA Paper 2011-3851, 20th AIAA Computational Fluid Dynamics Conference, Honolulu, Hawaii , June 2011.

[8]Chan, W. M., Gomez, R. J., Rogers, S. E., Buning, P. G., "Best Practices in Overset Grid Generation", AIAA Paper 2002-3191, The 32nd AIAA Fluid Dynamics Conference, St. Louis, Missouri, June 2002.

[9]Johnson, W., "Rotorcraft Aerodynamic Models for a Comprehensive Analysis", American Helicopter Society 54th Annual Forum, Washington, D. C., May 1998.

[10]Potsdam, M., Yeo, H., and Johnson, W., "Rotor Airloads Prediction Using Loose Aerodynamics/Structural Coupling", American Helicopter Society 60th Forum, Baltimore, Maryland, June 2004.

[11]Haimes, R., and Dannenhoffer, J. F., "The Engineering Sketch Pad: A Solid-Modeling, Feature-Based, Web-Enabled System for Building Parametric Geometry", AIAA Paper 2013-3073, The 21st AIAA Computational Fluid Dynamics Conference, San Diego, California, June 2013.

[12]Yoon, S., Chaderjian, N. M., Pulliam, T. H., and Holst, T. L., "Effect of Turbulence Modeling on Hovering Rotor Flows", AIAA Paper 2015-2766, The 45th AIAA Fluid Dynamics Conference, Dallas, Texas, June 2015.

[13]Yoon, S., Lee, H. C., and Pulliam, T. H., "Computational Analysis of Multi-Rotor Flows", AIAA Paper 2016-0812, The 54th AIAA Aerospace Sciences Meeting, AIAA SciTech Forum, San Diego, California, January 2016.

[14]Yoon, S. Lee, H. C., and Pulliam, T. H., "Computational Study of Flow Interactions in Coaxial Rotors", The AHS Technical Meeting on Aeromechanics Design for Vertical Lift, San Francisco, California, January 2016.

[15]Spalart, P. R., Jou, W-H., Strelets, M., and Allmaras, S. R., "Comments on the Feasibility of LES for Wings and on a Hybrid RANS/LES Approach", Advances in DNS/LES, Greyden Press, 1997, pp. 137-147.

[16]Spalart, P. R., "Strategies for Turbulence Modeling and Simulations", International Journal of Heat and Fluid Flow, 21, 2000, pp. 252-263.

[17]Chaderjian, N., "Navier-Stokes Simulation of UH-60A Rotor/Wake Interaction Using Adaptive Mesh Refinement", American Helicopter Society 73rd Annual Forum, Fort Worth, Texas, May 2017.